Keeney *et al. Microstructures* 2023;3:2023041
DOI: 10.20517/microstructures.2023.41

Microstructures

Research Article

Open Access

Check for updates

What lies beneath? Investigations of atomic force microscopy-based nano-machining to reveal sub-surface ferroelectric domain configurations in ultrathin films

Lynette Keeney, Louise Colfer, Debismita Dutta, Michael Schmidt, Guannan Wei

Tyndall National Institute, University College Cork, Cork T12 R5CP, Ireland.

Correspondence to: Dr. Lynette Keeney, Tyndall National Institute, University College Cork, Lee Maltings Complex, Dyke Parade, Cork T12 R5CP, Ireland. E-mail: lynette.keeney@tyndall.ie

How to cite this article: Keeney L, Colfer L, Dutta D, Schmidt M, Wei G. What lies beneath? Investigations of atomic force microscopy-based nano-machining to reveal sub-surface ferroelectric domain configurations in ultrathin films. *Microstructures* 2023;3:2023041. https://dx.doi.org/10.20517/microstructures.2023.41

Received: 13 Aug 2023 **First Decision:** 24 Aug 2023 **Revised:** 31 Aug 2023 **Accepted:** 5 Sep 2023 **Published:** 20 Oct 2023

Academic Editor: Shujun Zhang **Copy Editor:** Fangyuan Liu **Production Editor:** Fangyuan Liu

Abstract

Multiferroic materials, encompassing simultaneous ferroelectric and ferromagnetic polarization states, are enticing multi-state materials for memory scaling beyond existing technologies. Aurivillius phase B6TFMO ($Bi_6Ti_xFe_yMn_zO_{18}$) is a unique room temperature multiferroic material that could ideally be suited to future production of revolutionary memory devices. As miniaturization of electronic devices continues, it is crucial to characterize ferroelectric domain configurations at very small (sub-10 nm) thickness. Direct liquid injection chemical vapor deposition allows for frontier development of ultrathin films at fundamental (close to unit cell) dimensions. However, layer-by-layer growth of ultrathin complex oxides is subject to the formation of surface contaminants and 2*D* islands and pits, which can obscure visualization of domain patterns using piezoresponse force microscopy (PFM). Herein, we apply force from a sufficiently stiff diamond cantilever while scanning over ultrathin films to perform atomic force microscopy (AFM)-based nano-machining of the surface layers. Subsequent lateral PFM imaging of sub-surface layers uncovers 45° orientated striped twin domains, entirely distinct from the randomly configured piezoresponse observed for the pristine film surface. Furthermore, our investigations indicate that these sub-surface domain structures persist along the in-plane directions throughout the film depth down to thicknesses of less than half of an Aurivillius phase unit cell (< 2.5 nm). Thus, AFM-based nano-machining in conjunction with PFM allows demonstration of stable in-plane ferroelectric domains at thicknesses lower than previously determined for multiferroic B6TFMO. These findings demonstrate the

technological potential of Aurivillius phase B6TFMO for future miniaturized memory storage devices. Next-generation devices based on ultrathin multiferroic tunnel junctions are projected.

Keywords: Scanning probe microscopy, piezoresponse force microscopy, ultrathin films, chemical vapor deposition, ferroelectrics, multiferroics, atomic force microscopy-based nano-machining, domains, domain walls

INTRODUCTION

As miniaturization of electronic devices continues, a key condition for materials in memory storage technologies is the extension of their functional properties to ultrathin (sub-10 nm) thicknesses. This is challenging for multiferroics and ferroelectrics, given that ferroelectricity is a collective effect between competing short-range covalent repulsions and long-range Coulomb interactions. These interactions will alter as the collective distortion of unit cells (u.c.) within the lattice is adjusted on decreased thickness, and the spontaneous ferroelectric polarization is projected only to be supported above a particular critical thickness[1]. A consequence of fabricating low-dimensional ferroelectric nanostructures is an increase in surface area, which can result in enlarged depolarization field strengths (of magnitude inversely proportional to the thickness of the ferroelectric) if the surface charges are not completely screened. Below the critical thickness, out-of-plane ferroelectricity is destabilized, tending to a decline in performance and a lack of reproducibility. In 1997, this critical thickness was thought to be 20 nm[2]; however, considerable advancements in thin film synthesis and characterization over the last two decades[3] have enabled demonstration of stable out-of-plane ferroelectricity in high-quality ultrathin films at dimensions much thinner than this. Exploitation of epitaxial strain and confinement strain, along with effective screening of interface and surface charges, can counteract the opposing effects of thickness reduction and stabilize out-of-plane ferroelectricity at reduced dimensions. Out-of-plane ferroelectricity has been measured at a minimum thickness of 4 nm (10 u.c.) for $Pb(Zr_{0.2}Ti_{0.8})O_3$[4], 1.2 nm (3 u.c.) for $PbTiO_3$[5], 1 nm for $BaTiO_3$[6], and 1 nm (2 u.c.) for $Hf_{0.8}Zr_{0.2}O_2$[7].

Moreover, the problems pertaining to depolarization field effects are substantially diminished for in-plane polarization directions. Polarization is lateral to the surface for all in-plane directions and is, therefore, not impeded by contesting depolarization fields upon scaling down to ultrathin thicknesses[8]. A family of materials possessing large in-plane spontaneous polarizations [P_s ($\approx$ 0.4 C m^{-2})] are the Aurivillius phase materials described by the general formula $Bi_2O_2(A_{m1}B_mO_{3m+1}))$[9-14]. They are a well-established group of ferroelectrics and a technologically important class of material. $SrBi_2Ta_2O_9$ (m = 2) and $Bi_{3.25}La_{0.75}Ti_3O_{12}$ (m = 3) thin films have been exploited for commercial use in ferroelectric random access memory devices[15-18]. By intermixing differing types of *A*-site (Bi) and *B*-site (Ti, Mn, Fe) cations within the Aurivillius phase scaffold, the chemistries required for ferroelectricity and ferromagnetism can be combined in a single-phase to create the m = 5 B6TFMO($Bi_6Ti_xFe_yMn_zO_{18}$) composition (where x = 2.80 to 3.04; y = 1.32 to 1.52; z = 0.54 to 0.64). B6TFMO is a valuable example of a single-phase room temperature (RT) multiferroic joining other innovatively designed multiferroics such as the compositionally controlled tilt-engineered perovskites[19] and the 3*D* strained vertically aligned nanocomposites of polar and magnetic materials[20,21]. B6TFMO displays saturation magnetization (M_S) values (215 emu/cm^3) two orders of magnitude larger than widely-studied $BiFeO_3$[22] and demonstrates the reversible linear RT magnetoelectric switching necessary for practical applications in future high data-storage, multi-state memory storage devices[23,24]. Furthermore, B6TFMO thin films are capable of hosting extraordinary polarization profiles, including charged domain walls and non-trivial polar vortex-type topologies. This further opens up technological prospects in nano-electronics, domain wall devices, and ultra-compact data storage[25]. Aurivillius layer structures [Figure 1A] are innately two-dimensionally nanostructured with large c-axis lattice parameters (e.g., c = 50.26 Å for B6TFMO)[24]. Thus, they are ideal candidates for probing ferroelectric behavior close to the unit cell level[26-30].

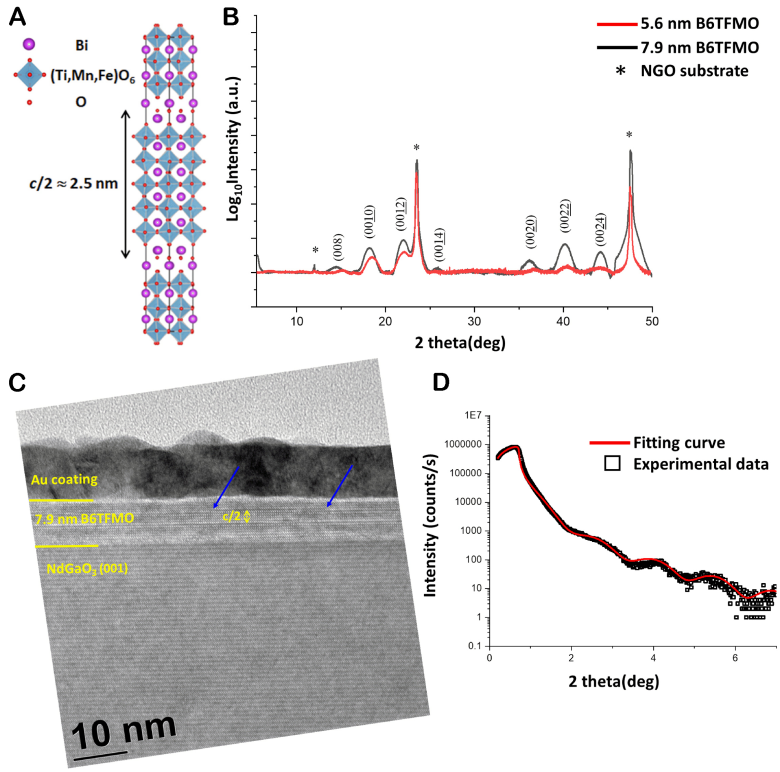

Figure 1. (A) Schematic of an *m* = 5 Aurivillius phase crystal structure (space group *B2eb*) projected down the <110> orientation[43,59]. Half a u.c. (*c*/2) consists of five perovskite blocks between fluorite-type bismuth oxide layers. (B) Representative XRD patterns of 7.9 nm and 5.6 nm B6TFMO films on NGO (001). (C) Representative HR-TEM image demonstrating 7.9 nm thick B6TFMO films on NGO (001) substrates. (D) XRR plot used to extract the thickness value of the 5.6 nm B6TFMO film on NGO (001).

It is widely acknowledged[31,32] that a ferroelectric domain structure is the initial governing factor in polarization switching behavior, influencing domain wall motion, evolution of existing ferroelectric domains, and the nucleation and development of further ferroelectric domains. The equilibrium domain configuration in a ferroelectric thin film arises from the minimization of the elastic and electrostatic energies in the crystal and is influenced by factors such as the film composition, growth mechanism, growth and cooling temperatures, underlying substrate, electrodes, and thin film thickness. Therefore, the characterization, understanding, and tailoring of ferroelectric domain structures in ultrathin films is imperative for controlling electromechanical properties and device applications. Piezoresponse force microscopy (PFM) is a powerful tool for probing ferroelectric phenomena at nanoscale and can reveal fundamental information on domain size, orientation, pattern, anisotropy/isotropy, and the nature of the domain walls that separate the ferroelectric domains. PFM experiments demonstrate that stable and switchable ferroelectricity persists in sub-8 nm Aurivillius B6TFMO films, initiating options for miniaturizing innovative multiferroic-based devices incorporating ultrathin tunnel junctions[27,28]. However, because B6TFMO thin film synthesis tends to proceed by a 2*D* nucleation and layer-by-layer growth mechanism[33], it can be difficult to control the formation of intermediary steps in the layer-by-layer growth mode, particularly at sub-10 nm film thickness. As a result, incomplete growth layers corresponding to heights of half of a unit cell of the Aurivillius phase (~2.5 nm thick) are visible on the film surface, complicating the surface PFM images and obscuring the ferroelectric domain configuration of the underlying B6TFMO film[24,27].

In recent years, AFM tip-based nano-machining has been recognized as an emerging technology for machining nanostructures, nanometer-scale 3*D* imaging of material properties and photomask repair[34-39]. In this contribution, we employ a commercially available probe to perform atomic force microscopy (AFM)-based nano-machining to remove surface artifacts and expose the underlying ferroelectric domain configuration of 7.9 nm (1.5 u.c.) and 5.6 nm (1 u.c.) B6TFMO films. We perform PFM investigations as a function of milled depth (from surface to substrate) to investigate domain structures and persistence of ferroelectricity through the ultrathin B6TFMO films.

MATERIALS AND METHODS

Ultrathin film synthesis

B6TFMO thin films were fabricated using a horizontal flow AIXTRON AIX 200/4FE AVD direct liquid injection chemical vapor deposition (DLI-CVD) system using processes similar to those previously described by Keeney *et al.*[27,28]. Bismuth, iron, and titanium precursor solutions [0.1 mol dm^{-3} solutions of $Bi(thd)_3$, $Fe(thd)_3$, and $Ti(O\text{-}iPr)_2(thd)_2$ (where thd = 2,2,6,6-tetramethyl 3,5-heptanedionate; O-iPr = isopropoxide) in toluene] were purchased from Epivalence Ltd. (The Wilton Centre, Redcar, Cleveland, TS10 4RF, United Kingdom) and were maintained under $N_2(g)$ in stainless steel bubbler containers. 0.025 mol dm^{-3} manganese precursor was prepared by dissolving $Mn(thd)_3$ (99%, STREM chemicals) in anhydrous toluene (99.8%, Sigma-Aldrich) under $N_2(g)$ and transferring to a stainless steel bubbler. The pressure of the growth chamber was 9 mbar, and the temperature of the susceptor [rotated with 60 sccm $N_2(g)$] heated substrate holder was maintained at 710 °C via an infra-red lamp assembly. The liquid precursors were injected using inert $N_2(g)$ carrier gas into a vaporizer kept at 220 °C, using four individual injectors, one for each precursor source. The micro-liter injected precursor volumes were regulated by tuning the numbers of pulses [between 75 and 100 injections for each precursor, depending on desired film thickness (between 5 nm and 8 nm)] and the opening time of the injectors (between 1.3 and 11.3 ms) during a continuous injection mode (frequency of 1 Hz). The net volumetric precursor ratios were approximately 2.9:1.5:0.6 for $Ti(O\text{-}iPr)_2(thd)_2$, $Mn(thd)_3$, and $Fe(thd)_3$, respectively. Between 5 and 8% excess of $Bi(thd)_3$ was utilized to mitigate bismuth migration during deposition. The total $N_2(g)/O_2(g)$ flow in the growth chamber was 3,000 sccm, of which $O_2(g)$ flow was 1,000 sccm. The substrates used in this study were single-side polished (001)-orientated $NdGaO_3$ (NGO) with average dimensions 10 mm × 10 mm × 0.5 mm (Crystal GmBH, Ostendstraße 25, D-12459 Berlin, Germany). The substrates were cleaned with isopropyl alcohol followed by distilled water and dried using $N_2(g)$.

Physical characterization

The crystallographic structure of the films was determined using a Panalytical MRD X-Pert Pro X-ray diffraction (XRD) system with a filtered Cu K radiation source (λ = 0.1541876 nm). The setup included a vertical magnetic strip mount, a 2 mm mask, and a divergence slit of 0.5°. Scans were conducted over a 2θ (2 theta) range of 5° to 50°, employing a precise step size of 0.006°. Each step was captured within 0.5 s, resulting in a total of 7,500 data points collected across the scan. To ensure accurate intensity comparisons, a uniform baseline correction was applied to both spectra using the second derivative method. Full Width at Half Maximum (FWHM) values for the peaks were established by integrating the peaks using a Gaussian function in the Origin software. The X-ray reflectivity (XRR) method was used to determine the film thickness of the B6TFMO film deposited using 75 injections. The same XRD system was used to detect the reflectometry on the ultrathin film and substrate. 2Theta-Omega scans were performed over an angular 2θ range of 0.2° to 7° with an angular $\Delta\theta$ step of 0.005°. A parabolic mirror was used as the incident optics, while a parallel plate collimator with a 0.09° slit was used as the diffracted optics. The XRR data was then analyzed through automatic fitting procedures implemented in the Panalytical XRR software package, where the number of layers, the density of each layer, their thickness, and the interface or surface roughness can be adjusted within a reasonable user-defined range. During the simulation, three layers were assumed:

the NGO substrate, the B6TFMO sample layer, and an extra oxidation layer on top (which is deemed reasonable, as the sample had been kept in the air after deposition). The initial density value inputted for the NGO substrate was taken from the datasheet provided by the substrate manufacturer (Crystal GmBH, Ostendstraße 25, D-12459 Berlin, Germany), and that for the B6TFMO sample was taken from that reported by Bartkowska *et al.* on the m = 5 Aurivillius phase compositions[40]. The deviation between the experimental data curve and the fitted curve was calculated to be 2.37%. The thickness values obtained from the XRR measurements were consistent with measurements obtained by transmission electron microscopy (TEM) imaging of previous samples prepared under similar DLI-CVD conditions[27,28]. Micro-structural analysis was performed by high-resolution TEM (HR-TEM) on a JEOL 2100 TEM, operated at 200 kV. To enable HR-TEM imaging, the samples were coated with gold to counteract charging, followed by coating with platinum to enable focused ion beam (FIB) cross sectioning. Cross-section lamellae were made using a FEI Helios Nanolab 600i DualBeam FIB-scanning electron microscope (FIB-SEM) (final thinning settings: 93 pA current at 30 kV, final polish settings: 47 pA current at 5 kV). Thickness analysis of the B6TFMO film deposited using 100 injections was performed from 55 measurements across a 7.6 μm wide lamella. The standard deviation (SD) variability of the dataset was ±0.4 nm. An atomic force microscope (AFM), Bruker Dimension Icon in PeakForce Tapping mode (with Bruker SCANASYST-AIR probes, Al reflex coated, 2 nm tip radius, 70 kHz resonant frequency) was used for topography analysis of the films. Film surface roughness and surface impurity volume fraction measurements were accomplished by carrying out AFM measurements (1 μm × 1 μm scan area) over five different areas of the sample surface. Average root mean square (RMS) roughness (nm) figures are provided, along with the SD variability of the dataset. Average volume fraction (vol.%) quantities were determined from impurity particle count area as a proportion of the scan area.

AFM-based nano-machining and PFM experiments

AFM-based nano-machining of the surfaces of the ultrathin B6TFMO films was achieved using an Asylum Research MFP-3D™ AFM by applying force from a sufficiently stiff diamond cantilever. NM-RC (single crystal diamond, Au reflex coated, < 10 nm tip radius, 486 kHz resonant frequency, boron-doped) probes, commercially available from Adama Innovations (c/o Republic of Work, 12 South Mall, Cork, T12 RD43, Ireland), were used for the AFM-based nano-machining studies. The normal loading force, F (N), was calculated using Hookes law, $F = kz$, where k is the spring constant (N/m), and z (m) is determined by multiplying the calibrated deflection sensitivity (m/V) by the setpoint (V) (the difference between photodiode signal when the cantilever is far from the surface and when it is at setpoint). The spring constant [1.89×10^2 (±8.39%) N/m] was calibrated via the Sader method[41] by performing a thermal tune (1,000 samples) in free air to measure the resonance frequency and the quality factor of the cantilever. Loading forces of between 1.86 μN and 5.59 μN were utilized for each scan in this work. Successive scans were performed over 8 μm × 8 μm areas at a scan frequency of 0.75 Hz to progressively machine through the sample from the film surface until the substrate was reached. A machining scan angle of 90° was utilized unless otherwise specified. The depths of the nano-machined areas were measured by performing line section height profiles of imaged areas. The measured RMS roughness values for the nano-machined areas of the 7.9 nm B6TFMO sample were, in general, rougher [values of 0.52 nm (SD = ±0.42 nm), 0.46 nm (SD = ±0.38 nm), 0.50 nm (SD = ±0.42 nm), and 0.57 nm (SD = ±0.48 nm) for depths of 0.7 nm, 2.0 nm, 3.8 nm, and 6.2 nm, respectively] compared with roughness values for the pristine B6TFMO surface [0.29 nm (SD = ±0.23 nm)], which may be due to fluctuations in composition, structures, and structural defects in the underlying film. Whereas, the measured RMS roughness values for the nano-machined areas of the 5.6 nm B6TFMO sample were, as expected, in general smoother [values of 0.66 nm(SD = ±0.51 nm), 0.09 nm (SD = ±0.07 nm), 0.08 nm (SD = ±0.07 nm), and 0.12 nm (SD = ±0.09 nm) for depths of 0.4 nm, 3.7 nm, 4.6 nm, and 5.3 nm, respectively] compared with roughness values for the pristine B6TFMO surface [0.37 nm (SD = ±0.27 nm)]. The roughness values for when nano-machining reached the underlying NGO

substrate were 0.09 nm (SD = ±0.07 nm) and 0.12 nm (SD = ±0.10 nm) for NGO underneath the 7.9 nm film and 5.6 nm film, respectively. Nanoscale electromechanical properties of the ultrathin films were evaluated by PFM using an Asylum Research MFP-3D™ AFM in contact mode in conjunction with a HVA220 Amplifier and a cantilever scan angle of 90°. The Dual AC (alternating current) Resonance Tracking PFM (DART-PFM) mode was utilized to amplify both the vertical and lateral piezo signals. Apex Super Sharp conductive diamond probes AD-2.8-SS (boron doped, Au reflex coated, < 5 nm tip radius, 75 kHz resonant frequency) were purchased from Adama Innovations (c/o Republic of Work, 12 South Mall, Cork, T12 RD43, Ireland) and used to image piezoelectric domains over 1 μm × 1 μm scan areas. Imaging of the same sample area by vertical PFM (Vert PFM) and lateral PFM (Lat PFM) enables corresponding measurements of the normal component of the piezoresponse vector (out-of-plane direction) and the transversal component of the in-plane piezoresponse (perpendicular to the cantilever axis), respectively[42]. The Lat PFM measurements were conducted by a comparable method to the Vert PFM measurements, except the "InFast" option was set to "Lateral" as opposed to "AC Deflection", respectively. The drive frequencies were operated near contact resonance for lateral (480 to 520 kHz) and vertical (250 to 280 kHz) modes. PFM measurements were operated at AC drive amplitudes (V_{AC}) of 4.0 V_{AC} and below.

RESULTS AND DISCUSSION

Characterization of structure, surface morphology, and surface piezo-configurations of as-prepared ultrathin B6TFMO films

Two different thicknesses of B6TFMO films were synthesized on (001)-orientated NGO substrates by pulsing either 75 injections or 100 injections of each precursor during the DLI-CVD process. The pseudo-cubic lattice parameter (a_p') of the perovskite-type layer in B6TFMO is 3.89 Å and a_p' is 3.858 Å for NGO; therefore, the lattice mismatch = -0.82%[27]. Out-of-plane XRD profiles, as shown in Figure 1B, are consistent with epitaxial films of an orthorhombic Aurivillius phase with five perovskite layers per half unit cell (m = 5) interleaved by bismuth oxide interfaces, as depicted schematically in Figure 1A[43]. Both B6TFMO films demonstrate a preference for orientating along the c-axis of the structure, with only (00l) Bragg reflections visible in the diffractograms. The broadening of the peaks [e.g., FWHM values for the (0010), (0012), and (0020) peaks are 1.721°, 0.400°, and 2.114° and are 1.534°, 0.389° and 1.186° for B6TFMO deposited with 75 injections and 100 injections, respectively] is due to grain size effects and due to the fact that the X-ray beam is scattering from only three, or less, half-unit cell repeat entities[44]. Comparative XRD patterns obtained from B6TFMO films deposited with 75 injections and 100 injections demonstrate that the intensities of the film deposited using 75 injections [e.g., the $\log_{10}$ intensity of the (0010), (0012), and (0020) peaks are: 0.461, 0.616, and 0.130 counts] are lower than the intensities of the film deposited using 100 injections [e.g., the $\log_{10}$ intensity of the (0010), (0012), and (0020) peaks are: 0.717, 0.951, and 0.371 counts], corresponding to a decreased film thickness for the film deposited using 75 injections. HR-TEM imaging [Figure 1C] confirms that the films have an m = 5 Aurivillius phase structure, displaying some regions with out-of-phase boundary defects and associated stacking faults (indicated by the blue arrows), typically observed for layered Aurivillius materials. This structural disorder within the samples would also contribute to peak broadening observed in the XRD profiles and might explain why there are additional variations in peak broadening between the 7.9 nm and 5.6 nm B6TFMO films [e.g., the FWHM value for the (008) reflection of the 7.9 nm film (1.079°) indicates that it is broader compared to the 5.6 nm film (0.970°)]. Contributions to the broadening of the asymmetric peaks may also result from segregation of secondary phases or crystal twinning, which will be discussed later. HR-TEM and XRR [Figure 1D] and [Supplementary Table 1] measurements yield average thickness values of 7.9 nm and 5.6 nm for B6TFMO films deposited using 100 injections and 75 injections, respectively. The former equates to a thickness of approximately 1.5 unit cells, and the latter equates to a thickness of approximately 1 unit cell of the m = 5 Aurivillius phase. These thickness measurements are consistent with previous TEM measurements of B6TFMO films prepared on different substrates under similar growth DLI-CVD conditions[27,28].

Epitaxial growth of layered Aurivillius phases under high supersaturation conditions is inclined to proceed via a 2*D* nucleation and layer-by-layer (Frank-Van der Merwe) growth mode[27-30,33,45], as illustrated in Figure 2A. Laterally grown layers with heights consistent with the lattice parameter of half of a u.c. of the Aurivillius structure evolve and increasingly merge and condense to form a complete (flat) layer prior to the nucleation of subsequent half-unit cell-thick layers. Each complete growth layer is ~2.5 nm in thickness for B6TFMO. Depending on the level of saturation during intermediary steps in the layer-by-layer growth mode, either 2*D* islands or pits (holes) can be seen on the film surface. The pits are referred to as "loch-keime" (hole-nuclei), which are "negative" 2*D* islands[33]. These types of 2*D* islands and pits are visible in the HR-TEM images in Figure 2B and the AFM image in Figure 2C for the 7.9 nm (1.5 u.c.) and 5.6 (1 u.c.) nm B6TFMO films. The coalescence of the laterally grown layers can be seen in Figure 2C, where the majority of the incomplete surface is covered by the growing 2-*D* layer, with darker regions in between corresponding to the underlying layer beneath ("negative" 2*D* islands). The height (depth) of these Aurivillius phase 2*D* islands (pits) is approximately 2.5 nm, corresponding to half a unit cell (*c*/2) of the $m = 5$ B6TFMO structure. AFM imaging with a sharp (2 nm tip radius) probe exposes other island-type surface contaminants present at a volume fraction of 6.7 vol.%. These surface features, encircled in red in [Figure 2C], appear to be spherical in nature and are < 20 nm in diameter. While the HR-TEM imaging and XRD analysis in this work could not identify the spherical surface features, it is possible that they correspond to spinel-type secondary phases identified in previous reports for films of this type[27,28]. Note that we have previously shown that these features can be reduced/eliminated by careful control of bismuth excess to counteract its volatility during growth[28].

DART-PFM imaging [Figure 2D] and [Supplementary Figure 1] utilizing a conducting diamond probe with an apex super sharp tip (radius < 5 nm) demonstrates that a random mixture of piezoresponse with indiscriminate orientation is exhibited for measurements of the pristine surface of the 7.9 nm (1.5 u.c.) thick B6TFMO film. 180 phase contrast is displayed for oppositely polarized domains, separated by curved domain walls. Lateral PFM imaging [Figure 2D] and [Supplementary Figure 1A-C] enables measurement of the in-plane polarization components[42], whereas vertical PFM images [Supplementary Figure 1D and E] provide information on the out-of-plane component. Average surface in-plane domain sizes of 440 nm^2 (SD = 1.6 × 10^3 nm^2) and out-of-plane domain sizes of 378 nm^2 (SD = 488 nm^2) are observed. Crystal symmetry of the $m = 5$ B6TFMO Aurivillius phase with an *odd* m number of perovskite layers determines that the major polarization vector primarily lies along the *a*-axis (in-plane, lateral direction). Only minor polarization is expected along the *c*-axis (out-of-plane, vertical direction)[46]; therefore, a relatively weaker piezoresponse (pm) is observed in the corresponding out-of-plane directed domains (Vert PFM images, [Supplementary Figure 1D and E]. The presence of non-ferroelectric spinel-type impurities did not seem to impact the local ferroelectric signal measured. However, these surface contaminants, in conjunction with surface Aurivillius phase 2*D* islands and pits, may have the effect of introducing varying tip-sample contact areas and obscuring orientated domain configurations corresponding to the underlying epitaxial B6TFMO film during surface PFM measurements.

Investigations of ferroelectric domain configuration in ultrathin B6TFMO as a function of AFM-based nano-machined depth

Progress in the miniaturization of semi-conductor processes has created an increased demand for AFM-based nanomachining to satisfy the role of defect removal with nano-meter level accuracy during photomask repair[37-39]. In this work, we apply the AFM-based nano-machining approach to remove surface contaminants from the ultra-thin B6TFMO films to uncover a complete Aurivillius phase surface layer. Successive scanning allows progressive nano-machining of the film at increased depths with nanometer-level control. A sufficiently stiff, commercially available diamond probe was used with a removal rate of between 0.13 nm/scan and 0.41 nm/scan.

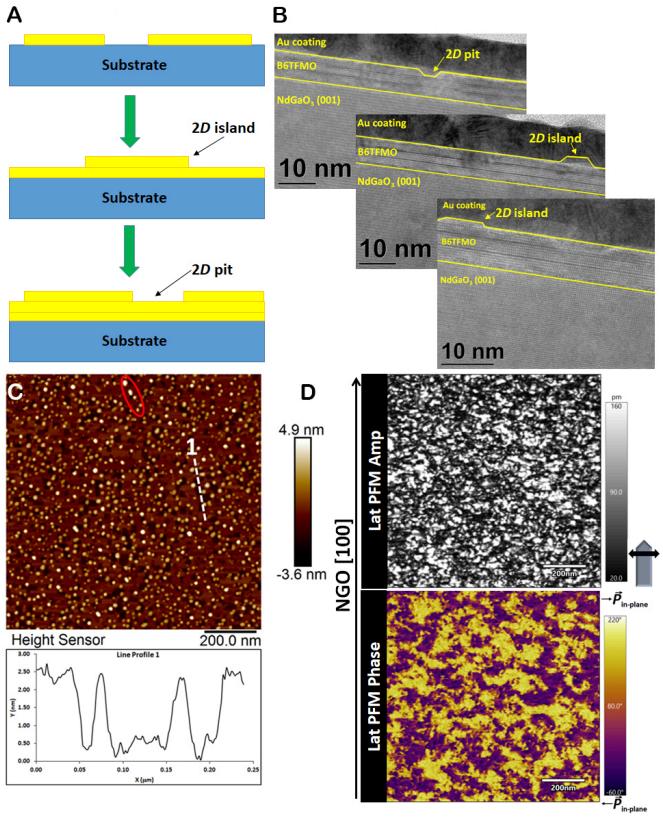

Figure 2. (A) A schematic of the 2*D* nucleation and layer-by-layer (Frank-Van der Merwe) growth mode. (B) Representative HR-TEM images demonstrating the presence of 2*D* islands and pits in the 7.9 nm thick B6TFMO film on NGO (001). (C) Representative AFM image of 5.6 nm thick B6TFMO film NGO (001) substrates. A line section profile 1 is shown in white through the 2D pits indicating a height of 2.5 nm, corresponding to half a u.c. (c/2) of the m = 5 Aurivillius structure (see Figure 1A). Small circular island-type inclusions (< 20 nm diameter) are encircled in red. (D) Lateral (Lat) PFM Amp and Phase images of the pristine surface of a 7.9 nm thick B6TFMO film.

Next, we performed PFM imaging of the 7.9 nm (1.5 u.c.) B6TFMO film as a function of nano-machined thickness. Lateral PFM results, scanned with the long-axis of the cantilever orientated parallel to the NGO [010] direction, are shown in Figure 3. While a randomly distributed piezoresponse without a favored domain orientation is observed for the pristine film surface [Figure 3A-C], on removal of 0.7 nm of the film surface [Figure 3D-F], it is revealed that spontaneous polarization orientates in distinct stripe domain configurations along the *a*-*b* plane, at 45° to the orthorhombic *b*-axis of NGO. Vertical PFM images [Supplementary Figure 2] demonstrate that a weaker component of the spontaneous polarization exists out of the *a*-*b* plane (along the *c*-axis). This observed vertical response is expected for an m = 5, an odd-layered Aurivillius phase[47]. The measured domain widths are of the order of 0.14 μm for the nano-machined 7.9 nm (1.5 u.c.) B6TFMO sample. The 45° stripe domains were observed to persist at nano-machined depths of 2.0 nm [Figure 3G-I], 3.8 nm [Figure 3J-L], and 6.2 nm [Figure 3M-O]. It is only until the sample is nano-machined all the way through the film to the underlying NGO substrate that the PFM signal is lost. Note that great care was taken to ensure that the striped domain features angled at 45° were not artifacts created by the nano-machining process. Nano-machining investigations using intentionally aggressive load forces as a function of nano-machining angle (0°, 45°, 90°) were performed to distinguish the deliberately-created scan artifacts from the 45° stripe domains inherent to the B6TFMO films. Details establishing that 45° stripe ferroelectric domains are independent of topography and nano-machining scan artifacts are described in the Supplementary Material and Supplementary Figure 3.

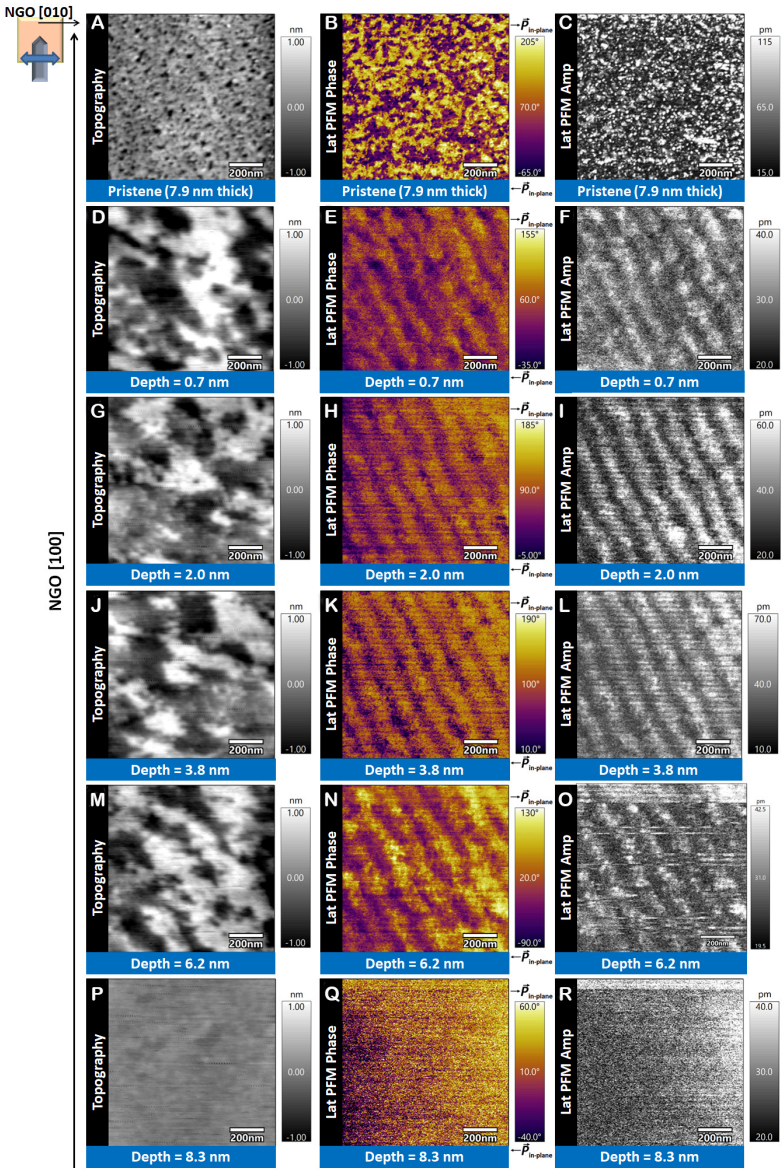

Figure 3. Representative topography and lateral (lat) DART-PFM phase and amplitude (amp) images of 7.9 nm (1.5 u.c.) B6TFMO on NGO (001) as a function of AFM-based nano-machined depth. The scanning direction of the cantilever was parallel with the $[010]_{substrate}$ axis.

Gradauskaite *et al.*[29,30] and Keeney *et al.*[27] previously observed stripe domains for one u.c. thick (5 nm) Aurivillius phase films that were terminated with complete Aurivillius layers and exhibited an atomically flat surface. It was deemed that domain patterns are stabilized by the underlying NGO substrate, where the lattice mismatch is progressively lost as film thickness increases. For films of two unit cells in thickness, an isotropic random distribution of 180° domains was observed[29,30]. Therefore, the question arises as to whether the onset of 45° striped domain observation in this work happens solely due to the ability to image the B6TFMO film at decreased thickness, where the domain patterns are possibly stabilized by substrate strain effects. Alternatively, the onset of striped domain observation from the nano-machining process may be due to the removal of otherwise masking surface 2D islands, pits, and contaminants to reveal a smooth B6TFMO surface terminated with a complete Aurivillius layer.

To distinguish between the two possibilities, PFM imaging was performed on the thinner 5.6 nm (1 u.c.) B6TFMO film, prepared by the same layer-by-layer growth process as the 7.9 nm (1.5 u.c.) thick B6TFMO film. Lateral DART-PFM images, scanned with the long-axis of the cantilever orientated parallel to the NGO [100] direction, are shown in Figure 4. Based on the results of the 7.9 nm (1.5 u.c.) thick B6TFMO films in Figure 3G-I, where the milled depth corresponds to a thickness of 5.9 nm and results from previous 5 nm-thick B6TFMO films exhibiting an atomically flat surface[27], we would expect to see 45° striped domain patterns for the 5.6 nm (1 u.c.) B6TFMO film. However, a random mixture of piezoresponse with indiscriminate orientation is exhibited for measurements of the pristine surface of the 5.6 nm (1 u.c.) thick B6TFMO film, as shown in Figure 4A-C. 180 degree phase contrast is displayed for oppositely polarized domains with average surface in-plane domain sizes of 209 nm^2 (SD = 274 nm^2). Therefore, the observation of the randomly distributed piezoresponse in this work is due to the surface 2*D* islands, pits, and contaminants complicating the surface PFM signal. Stripe domain configurations along the *a*-*b* plane, at 45° to *b*-axis of the orthorhombic unit cell of NGO, are uncovered by PFM imaging on removal of surface contaminants by nanomachining at depths of 0.4 nm [Figure 4D-F], 3.7 nm [Figure 4G-I], 4.6 nm [Figure 4J-L], and 5.3 nm [Figure 4M-O]. We deduce that for the pristine film surfaces imaged in this work, the ferroelectric domains are not themselves inherently isotropic-type domains. Rather, the PFM probe is accessing fragmented Aurivillius phase structures (2*D* islands and pits); therefore, the piezoresponse and orientation cannot be visualized as continuous at the pristine surface. The differences in piezo-configuration between the pristine surface and exposed sub-surfaces can be attributed to the effectiveness of AFM-based nano-machining in removing growth surface artifacts, which, otherwise, obscure the domain configurations of the underlying planar B6TFMO film.

The measured domain widths are of the order of 0.08 μm for the nano-machined 5.6 nm (1 u.c.) B6TFMO sample; narrower than that observed for the thicker 7.9 nm (1.5 u.c.) B6TFMO sample, consistent with the Landau-Lifshitz-Kittel scaling law[48-50]. In the PFM images, striped domains are directed from the top left to the bottom right in the 7.9 nm (1.5 u.c.) B6TFMO sample where the PFM cantilever was aligned parallel to the [010] substrate direction, whereas domains are directed from top right to bottom left in the 5.6 nm (1 u.c.) B6TFMO sample, which was turned 90° so that the PFM cantilever was aligned parallel with the [100] NGO substrate direction. Topography images [Figure 4D] of the sample machined to a depth of 0.4 nm demonstrate that machining is somewhat "patchy" [with an RMS roughness value of 0.66 nm (±0.51 nm)] and did not completely remove the surface contaminants. PFM imaging [Figure 4E and F] shows a mixed image of domains with undefined orientation and 45° orientated stripe domains. Topography images [Figure 4M] of the sample machined to a depth of 5.3 nm show faint horizontal lines, which are scan artifacts of the nano-machining process as the film to substrate interface is approached. Remarkably, 45° striped domains and piezoresponse are also observed at this depth, which corresponds to less than half of an Aurivillius phase unit cell (< 2.5 nm). The nano-machining horizontal artifacts become more visible at machined depths of 7.2 nm [Figure 4P-R], correlating with the machining of the underlying NGO substrate and a loss in PFM signals. The 45° stripe domain configurations along the lateral *a*-*b* plane were observed to persist through the film, disappearing at depths consistent with the substrate. This is an interesting observation, as it suggests that the ferroelectric critical size limit may be absent for in-plane polarization directions in B6TFMO, similar to observations in optimized HfO_2 and $BiFeO_3$ films and thickness-dependent tomographic PFM studies of m = 4 Aurivillius phase films[7,51,52]. However, more detailed experiments correlating precise thickness measurements (e.g., using aberration-corrected scanning TEM) with PFM experiments are required in order to confirm whether or not a critical thickness exists for in-plane ferroelectricity in B6TFMO.

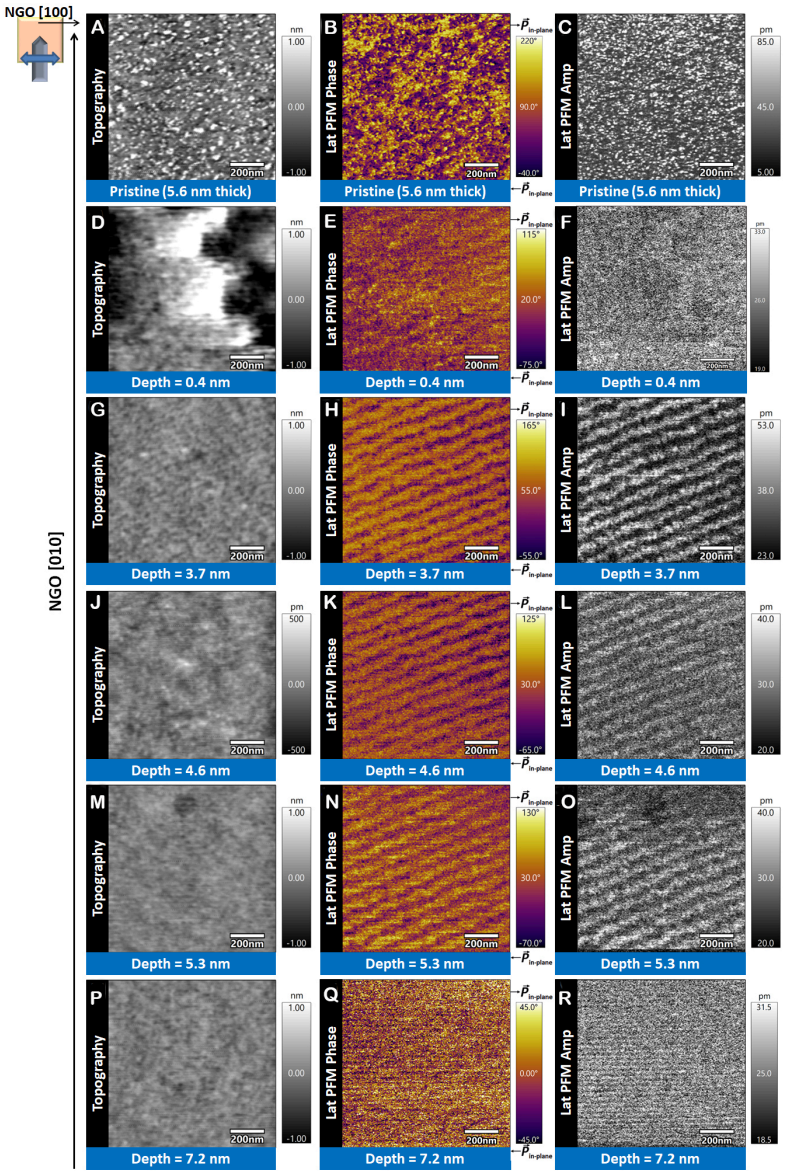

Figure 4. Representative topography and lateral (lat) DART-PFM phase and amplitude (amp) images of 5.6 nm (1 u.c.) B6TFMO on NGO (001) as a function of AFM-based nano-machined depth. The scanning direction of the cantilever scanning direction was parallel with the $[100]_{substrate}$ axis.

Crystal symmetry of the Aurivillius phases dictates that the major in-plane spontaneous polarization component lies entirely along the *a* axis (with a minor polarization along the out-of-plane *c*-axis in odd-layered structures)[43]. Therefore, there must be another physical origination for the experimentally observed 45° striped domains. *a-b* crystal twinning is a common occurrence in layered materials such as the layered high temperature superconductors[53] and Aurivillius phases[54]. The lack of uniaxial polarization in this work indicates that crystal twinning is present in the B6TFMO thin films. The crystal twinning would originate from the orthorhombic crystal structure of the underlying (001) NGO substrate, which presents an anisotropic template for growth based on a pseudo-cubic unit cell[53]. The *a* axis of the pseudo-cubic cell lies along the *ab* diagonals of the orthorhombic NGO crystal structure, and a pseudo-cubic lattice constant of 3.858 Å is presented for NGO. This provides a close lattice match to the a_p' of B6TFMO (3.89 Å) to grow

under minimal strain[27]; however, the angular anisotropy of the pseudo-cubic template would likely give rise to preferential twinning. The experimental observations of 45 orientated stripe domains, rather than expected in-plane uniaxial anisotropy, may be the result of crystal twinning in B6TFMO created by mimicking the pseudo-cubic symmetry of the underlying NGO substrate.

CONCLUSIONS

In summary, we demonstrate the use of AFM-based nano-machining using a commercially available diamond probe to remove surface contaminants from ultrathin B6TFMO films with nanometer-level precision. Complete Aurivillius layers are uncovered beneath the as-grown surface, with subsequent lateral PFM imaging revealing distinct stripe domain configurations along the *a*-*b* plane (at 45° to the NGO substrate *b*-axis), of stark contrast to the randomly distributed piezoresponse observed for the pristine film surface. We attribute the differences in piezo-configuration between the pristine surface and exposed sub-surfaces to the effectiveness of AFM-based nano-machining in removing growth surface artifacts (fractional Aurivillius phase 2*D* islands/pits and secondary phase contaminants) that, otherwise, mask the domain configurations of the underlying planar B6TFMO film. The experimental observations of 45° orientated stripe domains rather than in-plane uniaxial anisotropy are likely ensuing from the presence of crystal twinning in B6TFMO to conform to the pseudo-cubic symmetry of the underlying NGO substrate. The width of the 45° stripe domains is narrower for the 5.6 nm B6TFMO films (0.08 μm) compared to the 7.9 nm B6TFMO films (0.14 μm), consistent with the Landau-Lifshitz-Kittel scaling law[48-50]. Moreover, while previous PFM investigations of multiferroic m = 5 B6TFMO films demonstrated the persistence of stable ferroelectricity close to the unit cell level (5 nm to 8 nm)[27,28], the AFM-based nano-machining investigations in this work indicate that ferroelectricity persists at thicknesses lower than this. Stable sub-surface ferroelectric domain structures and piezoresponses persist along the in-plane directions throughout the film depth, down to less than half of an Aurivillius phase unit cell (< 2.5 nm). These findings, along with evidence for sub-unit cell ferroelectricity in exfoliated flakes[26] and planar thin films[29] of m = 4 Aurivillius phases, demonstrate the technological potential of Aurivillius phase B6TFMO for future miniaturized memory storage devices. For example, devices based on in-plane tunnel junctions are an appealing prospect, as they would not be expected to be obstructed by opposing depolarization fields upon thickness-scaling to ultrathin dimensions. This means that higher tunnelling current ratios could be achieved with non-destructive read processes. To date, no such in-plane devices have been commercialized; only theoretical device models based on monochalcogenides have been reported. However, it is difficult to synthesize high-quality ultra-thin monochalcogenides by scalable growth methods[55-58]. As such, optimized multiferroic B6TFMO Aurivillius phases, which can be synthesized by scalable DLI-CVD growth methods, are perfect candidates for utilization in next-generation devices based on ultrathin multiferroic tunnel junctions.

DECLARATIONS

Acknowledgments

The authors gratefully acknowledge the support of the Royal Society-Science Foundation Ireland (SFI) University Research Fellowship URF\R\201008 and the SFI Frontiers for the Future Project 19/FFP/6475.

Authors' contributions

Conceiving and coordinating the project, developing the DLI-CVD processes, synthesizing the ultra-thin B6TFMO thin films, and performing AFM and PFM characterization and AFM-based nanomachining experiments; interpreting the results in discussion with the other authors; initially writing of the first draft of the manuscript, with the final version being crafted through contributions from all authors: Keeney L
Making substantial contributions to the conception and design of the AFM-based nanomachining studies: Colfer L

Performing XRD characterization and interpreting the ultrathin B6TFMO films: Dutta D
Conducting FIB cross-sectioning of lamellae for TEM and performing HR-TEM analysis of the B6TFMO thin films: Schmidt M
Handling XRR analysis and interpretating the ultrathin B6TFMO films: Wei G
All authors have given their approval to the final version of the manuscript.

Availability of data and materials
The accepted publication is available on the open access University College Cork (UCC) CORA repository (https://cora.ucc.ie/).

Financial support and sponsorship
This work was supported by the Royal Society-Science Foundation Ireland (SFI) University Research Fellowship URF\R\201008 and the SFI Frontiers for the Future Project 19/FFP/6475.

Conflicts of interest
All authors declared that there are no conflicts of interest.

Ethical approval and consent to participate
Not applicable.

Consent for publication
Not applicable.

REFERENCES
1. Scott JF. Future issues in ferroelectric miniaturization. *Ferroelectrics* 1998;206:365-79. DOI
2. Li S, Eastman JA, Vetrone JM, Foster CM, Newnham RE, Cross LE. Dimension and size effects in ferroelectrics. *Jpn J Appl Phys* 1997;36:5169. DOI
3. Qiao H, Wang C, Choi WS, Park MH, Kim Y. Ultra-thin ferroelectrics. *Mater Sci Eng R Rep* 2021;145:100622. DOI
4. Tybell T, Ahn CH, Triscone J. Ferroelectricity in thin perovskite films. *Appl Phys Lett* 1999;75:856-8. DOI
5. Fong DD, Stephenson GB, Streiffer SK, et al. Ferroelectricity in ultrathin perovskite films. *Science* 2004;304:1650-3. DOI
6. Choi KJ, Biegalski M, Li YL, et al. Enhancement of ferroelectricity in strained BaTiO3 thin films. *Science* 2004;306:1005-9. DOI
7. Cheema SS, Kwon D, Shanker N, et al. Enhanced ferroelectricity in ultrathin films grown directly on silicon. *Nature* 2020;580:478-82. DOI
8. Vasudevan RK, Matsumoto Y, Cheng X, et al. Deterministic arbitrary switching of polarization in a ferroelectric thin film. *Nat Commun* 2014;5:4971. DOI
9. Guo YY, Gibbs AS, Perez-Mato JM, Lightfoot P. Unexpected phase transition sequence in the ferroelectric $Bi_4Ti_3O_{12}$. *IUCrJ* 2019;6:438-46. DOI PubMed PMC
10. Deepak N, Zhang PF, Keeney L, Pemble ME, Whatmore RW. Atomic vapor deposition of bismuth titanate thin films. *J Appl Phys* 2013;113:187207. DOI
11. Keeney L, Groh C, Kulkarni S, Roy S, Pemble ME, Whatmore RW. Room temperature electromechanical and magnetic investigations of ferroelectric Aurivillius phase $Bi_5Ti_3(FexMn_{1-x})O_{15}$ (x = 1 and 0.7) chemical solution deposited thin films. *J Appl Phys* 2012;112:024101. DOI
12. Keeney L, Kulkarni S, Deepak N, et al. Room temperature ferroelectric and magnetic investigations and detailed phase analysis of Aurivillius phase $Bi_5Ti_3Fe_{0.7}Co_{0.3}O_{15}$ thin films. *J Appl Phys* 2012;112:052010. DOI
13. Keeney L, Zhang PF, Groh C, Pemble ME, Whatmore RW. Piezoresponse force microscopy investigations of Aurivillius phase thin films. *J Appl Phys* 2010;108:042004. DOI
14. Zhang PF, Deepak N, Keeney L, Pemble ME, Whatmore RW. The structural and piezoresponse properties of *c*-axis-oriented Aurivillius phase $Bi_5Ti_3FeO_{15}$ thin films deposited by atomic vapor deposition. *Appl Phys Lett* 2012;101:112903. DOI
15. Wouters DJ, Maes D, Goux L, et al. Integration of $SrBi_2Ta_2O_9$ thin films for high density ferroelectric random access memory. *J Appl Phys* 2006;100:051603. DOI

16. Park BH, Kang BS, Bu SD, Noh TW, Lee J, Jo W. Lanthanum-substituted bismuth titanate for use in non-volatile memories. *Nature* 1999;401:682-4. DOI
17. Annual report pursuant to section 13 or 15(d) of the securities exchange act of 1934 for the fiscal year ended March 31, 2006 commission file number 1 - 6784. Available from: https://www.sec. gov/Archives/edgar/data/63271/000119312506188347/d20f.htm [Last accessed on 16 Oct 2023].
18. Fujii E, Uchiyama K. First 0.18 μm SBT-based embedded FeRAM technology with hydrogen damage free stacked cell structure. *Integr Ferroelectr* 2003;53:317-23. DOI
19. Pitcher MJ, Mandal P, Dyer MS, et al. Magnetic materials. Tilt engineering of spontaneous polarization and magnetization above 300 K in a bulk layered perovskite. *Science* 2015;347:420-4. DOI
20. Suwardi A, Prasad B, Lee S, et al. Turning antiferromagnetic $Sm_{0.34}Sr_{0.66}MnO_3$ into a 140 K ferromagnet using a nanocomposite strain tuning approach. *Nanoscale* 2016;8:8083-90. DOI
21. Choi EM, Maity T, Kursumovic A, et al. Nanoengineering room temperature ferroelectricity into orthorhombic $SmMnO_3$ films. *Nat Commun* 2020;11:2207. DOI PubMed PMC
22. Srihari NV, Vinayakumar KB, Nagaraja KK. Magnetoelectric coupling in bismuth ferrite - challenges and perspectives. *Coatings* 2020;10:1221. DOI
23. Keeney L, Maity T, Schmidt M, et al. Magnetic field-induced ferroelectric switching in multiferroic aurivillius phase thin films at room temperature. *J Am Ceram Soc* 2013;96:2339-57. DOI
24. Faraz A, Maity T, Schmidt M, et al. Direct visualization of magnetic-field-induced magnetoelectric switching in multiferroic aurivillius phase thin films. *J Am Ceram Soc* 2017;100:975-87. DOI
25. Moore K, O'Connell EN, Griffin SM, et al. Charged domain wall and polar vortex topologies in a room-temperature magnetoelectric multiferroic thin film. *ACS Appl Mater Interfaces* 2022;14:5525-36. DOI PubMed PMC
26. Keeney L, Smith RJ, Palizdar M, et al. Ferroelectric behavior in exfoliated 2D aurivillius oxide flakes of sub-unit cell thickness. *Adv Elect Materials* 2020;6:1901264. DOI
27. Keeney L, Saghi Z, O'sullivan M, Alaria J, Schmidt M, Colfer L. Persistence of ferroelectricity close to unit-cell thickness in structurally disordered aurivillius phases. *Chem Mater* 2020;32:10511-23. DOI
28. Keeney L, Colfer L, Schmidt M. Probing ferroelectric behavior in sub-10 nm bismuth-rich aurivillius films by piezoresponse force microscopy. *Microsc Microanal* 2022;28:1396-406. DOI
29. Gradauskaite E, Campanini M, Biswas B, et al. Robust in-plane ferroelectricity in ultrathin epitaxial aurivillius films. *Adv Materials Inter* 2020;7:2000202. DOI
30. Gradauskaite E, Gray N, Campanini M, Rossell MD, Trassin M. Nanoscale design of high-quality epitaxial aurivillius thin films. *Chem Mater* 2021;33:9439-46. DOI
31. Wang Y, Chen W, Wang B, Zheng Y. Ultrathin ferroelectric films: growth, characterization, physics and applications. *Materials* 2014;7:6377-485. DOI PubMed PMC
32. Lines ME, Glass AM. Principles and applications of ferroelectrics and related materials. Oxford: Oxford University Press; 1977. p.525. Available from: https://academic.oup.com/book/25990 [Last accessed on 11 Oct 2023].
33. Venables JA, Spiller GDT, Hanbucken M. Nucleation and growth of thin films. *Rep Prog Phys* 1984;47:399. DOI
34. Binnig G, Quate CF, Gerber C. Atomic force microscope. *Phys Rev Lett* 1986;56:930-3. DOI PubMed
35. Steffes JJ, Ristau RA, Ramesh R, Huey BD. Thickness scaling of ferroelectricity in $BiFeO_3$ by tomographic atomic force microscopy. *Proc Natl Acad Sci USA* 2019;116:2413-8. DOI PubMed PMC
36. Wang J, Yan Y, Li Z, Geng Y, Luo X, Fan P. Processing outcomes of atomic force microscope tip-based nanomilling with different trajectories on single-crystal silicon. *Precis Eng* 2021;72:480-90. DOI
37. Iwata F, Saigo K, Asao T, et al. Removal method of nano-cut debris for photomask repair using an atomic force microscopy system. *Jpn J Appl Phys* 2009;48:08JB20. DOI
38. Robinson T, Dinsdale A, Bozak R, White R, Archuletta M. Nanomachining processes for 45, 32 nm mode mask repair and beyond. Procedings of the Photomask and Next-Generation Lithography Mask Technology XV; 2008 May 19; Yokohama, Japan. DOI
39. Robinson T, Dinsdale A, Bozak R, Arruza B. Advanced mask particle cleaning solutions. Procedings of the SPIE Photomask Technology; 2007 Oct 30; Monterey, United States. DOI
40. Bartkowska JA, Bochenek D, Niemiec P. Multiferroic aurivillius-type $Bi_6Fe_{2-x}Mn_xTi_3O_{18}$ ($0 \leq x \leq 1.5$) ceramics with negative dielectric constant. *Appl Phys A* 2018;124:823. DOI
41. Sader JE, Borgani R, Gibson CT, et al. A virtual instrument to standardise the calibration of atomic force microscope cantilevers. *Rev Sci Instrum* 2016;87:093711. DOI
42. Kalinin SV, Rodriguez BJ, Jesse S, et al. Vector piezoresponse force microscopy. *Microsc Microanal* 2006;12:206-20. DOI
43. Ismunandar, Kamiyama T, Hoshikawa A, et al. Structural studies of five layer Aurivillius oxides: $A_2Bi_4Ti_5O_{18}$ (A = Ca, Sr, Ba and Pb). *J Solid State Chem* 2004;177:4188-96. DOI
44. Holder CF, Schaak RE. Tutorial on powder X-ray diffraction for characterizing nanoscale materials. *ACS Nano* 2019;13:7359-65. DOI PubMed
45. Frank FC, van der Merwe JH. One-dimensional dislocations III. Influence of the second harmonic term in the potential representation, on the properties of the model. Proceedings of the Royal Society of London; 1949 Dec 22; London, UK. London: Royal; pp. 125-34.
46. Trolier-mckinstry S. Crystal chemistry of piezoelectric materials. In: Safari A, Akdoğan EK, editors. Piezoelectric and acoustic materials for transducer applications. Boston: Springer US; 2008. pp. 39-56. DOI

47. Whatmore, R. Ferroelectric materials. In: Kasap S, Capper P, editors. Springer handbook of electronic and photonic materials. Springer International Publishing: Cham; 2017. p. 1. DOI
48. Landau L, Lifshitz E. 3 - on the theory of the dispersion of magnetic permeability in ferromagnetic bodies. In: Pitaevski LP editors. Perspectives in theoretical physics. The collected papers of E. M. Lifshitz. Amsterdam:Elsevier; 1992. pp. 51-65. DOI
49. Kittel C. Theory of the structure of ferromagnetic domains in films and small particles. *Phys Rev* 1946;70:965. DOI
50. Kittel C. Physical theory of ferromagnetic domains. *Rev Mod Phys* 1949;21:541. DOI
51. Wang H, Liu ZR, Yoong HY, et al. Direct observation of room-temperature out-of-plane ferroelectricity and tunneling electroresistance at the two-dimensional limit. *Nat Commun* 2018;9:3319. DOI PubMed PMC
52. Gradauskaite E, Meier QN, Gray N, et al. Defeating depolarizing fields with artificial flux closure in ultrathin ferroelectrics. *arXiv* 2022:2212;11073. DOI
53. Nam J, Hughes RA, Castellan JP, Gaulin BD, Britten JF, Preston JS. The origin of preferential twinning in $YBa_2Cu_3O_{7-\delta}$ thin films deposited on the (0 0 1) $NdGaO_3$ substrate. *J Appl Phys* 2005;97:123906. DOI
54. Zurbuchen MA, Cahill DG, Schubert J, Jia Y, Schlom DG. Determination of the thermal conductivity tensor of the $n = 7$ Aurivillius phase $Sr_4Bi_4Ti_7O_{24}$. *Appl Phys Lett* 2012;101:021904. DOI
55. Shen XW, Fang YW, Tian BB, Duan CG. Two-dimensional ferroelectric tunnel junction: the case of monolayer in:SnSe/SnSe/Sb:SnSe homostructure. *ACS Appl Electron Mater* 2019;1:1133-40. DOI
56. Chang K, Liu J, Lin H, et al. Discovery of robust in-plane ferroelectricity in atomic-thick SnTe. *Science* 2016;353:274-8. DOI
57. Liu J, Chang K, JI SH, Chen X, Fu L. Apparatus and methods for memory using in-plane polarization. Available from: https://www.osti.gov/servlets/purl/1438442 [Last accessed on 11 Oct 2023].
58. Shen H, Liu J, Chang K, Fu L. In-plane ferroelectric tunnel junction. *Phys Rev Appl* 2019;11:024048. DOI
59. Momma K, Izumi F. *VESTA 3* for three-dimensional visualization of crystal, volumetric and morphology data. *J Appl Cryst* 2011;44:1272-6. DOI